



Effect of fiber entanglement in chopped glass fiber reinforced composite manufactured via long fiber spray-up molding

Ji Ho Jeon^{a,b,1}, Chang Ki Yoon^{c,1}, Ying-Jun Quan^b, Jun Young Choi^c,
Sungjin Hong^c, Woo Il Lee^c, Kui-Kam Kwon^b, Sung-Hoon Ahn^{b,c,*}

^a George W. Woodruff School of Mechanical Engineering, Georgia Institute of Technology, Atlanta, GA, United States

^b Institute of Advanced Machines and Design, Seoul National University, South Korea

^c Department of Mechanical Engineering, Seoul National University, South Korea

ARTICLE INFO

Keywords:

Long fiber spray-up molding
Fiber entanglement
Composite fabrication
Image processing

ABSTRACT

Long Fiber Spray-up Molding (LFSM) deviates from the conventional approach in liquid composite molding (LCM) processes by utilizing extremely long chopped strands of fibers as the primary reinforcement material in its fabrication process. In LFSM, chopped fibers are impregnated with resin that is sprayed vertically downwards before reaching the mold surface. The spraying mechanism is mounted on an actuator, which is capable of spraying freely in any specified pattern or direction. Under LFSM, it is extremely difficult to fabricate a composite part with uniformly distributed fiber content throughout its volume. The consequences of the non-uniform fiber volume distribution arise from the fiber entanglement as the length of the fiber reaches up to 100 mm in LFSM. In this study, the effect of fiber entanglement during LFSM was analyzed through various approaches. This included measuring the coefficient of friction between fibers in contact and examining the correlation between fiber lengths and the number of intersections. Furthermore, the viscoelastic properties of the uncured composite part were assessed by experimenting with the influence of viscosity on fiber length during compression molding. The results were then computed, modeled, and visualized in MATLAB, considering variations in viscosity and fiber length, both before and after compression molding.

1. Introduction

Incorporation of autoclaves in the fabrication of composites results in high manufacturing costs and low production rates [1]. As industries seek to minimize production costs, alternative composite fabrication methods have been researched, developed, and implemented [2]. Among them, composites manufactured via liquid composite molding (LCM) processes have become more attractive owing to their high productivity and low manufacturing cost. In particular, resin transfer molding (RTM) is a widely known example of LCM [3]. Similar to RTM, structural reaction injection molding (S-RIM) can be classified as an LCM method, in which a preform of continuous fibers is placed prior to the mold closing for the resin to be injected for fiber impregnation [4]. For composite parts requiring less demanding mechanical performance in comparison to those fabricated by S-RIM, reinforced reaction injection molding (R-RIM), in which pre-mixed reinforcement fillers (milled or chopped strands) are injected with the resin into a closed mold, is used.

* Corresponding author. Institute of Advanced Machines and Design, Seoul National University, South Korea.

E-mail address: ahnsh@snu.ac.kr (S.-H. Ahn).

¹ Equally Contributed.

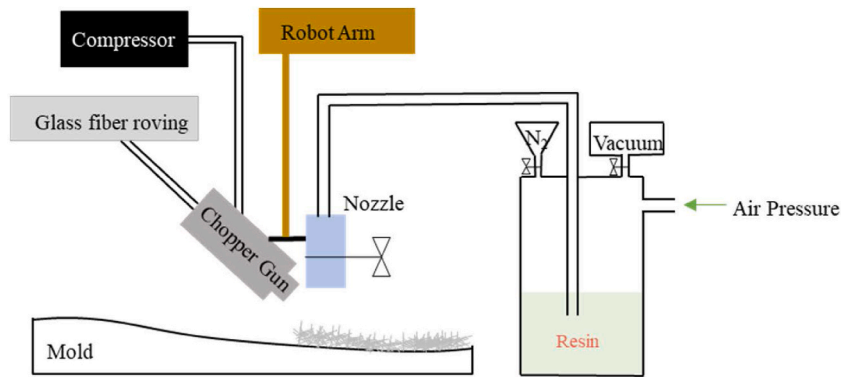


Fig. 1. Long Fiber Spray-up Molding schematic diagram.

Their lightweight potential and cost-effective production of intricate geometries at high volume make them advantageous for manufacturing components and structural parts [5]. Although R-RIM has several advantages, including a reduction of capital cost over the conventional RIM, it has some limitations, including unpredictable fiber orientation, limited fiber length, large viscosity increase, and significant wear of machinery parts [6]. Furthermore, although the manufacturing cost can be cut down by implementing R-RIM, the mechanical properties of continuous fiber reinforced composites (S-RIM) are superior over short discontinuous fiber reinforced composite parts (R-RIM).

Long Fiber Spray-up Molding (LFSM) is a fabrication method, in which chopped strands of glass fiber are deposited with a thermoset resin matrix onto an open mold [7]. Chopped glass fibers are pre-impregnated before reaching the mold surface through contact with the sprayed resin flowing vertically downwards. The viscous mixture is then compression molded to form the final shape. This molding process is significantly more advantageous over R-RIM since extremely long chopped fibers of lengths over 50 mm can be used. Furthermore, the quasi-isotropic nature of randomly distributed chopped strands of glass fibers with a length hundreds of times their critical length enables the composite part to reach a tensile strength up to almost 90 % of the continuous fiber regardless of the type of matrix [8]. For example, chopped carbon fiber/epoxy composite with 50 mm fiber length and 50 % fiber volume fraction reaches a tensile strength of up to 500 MPa, which is similar to that of continuous fiber reinforced composites manufactured with quasi-isotropic layout [9,10]. Furthermore, the use of long discontinuous fibers generally provides superior mechanical properties over short fibers due to the bridging effect as they stride along and aggregate [11]. This fabrication method is however limited by fiber entanglement due to extreme fiber lengths [12]. The entanglement causes unequal volume distribution of fibers in the composite part because the adhesion force of bonded fibers exceeds the viscous force of the resin upon compression molding [7]. Furthermore, the use of a low-viscosity resin requires significant precaution because under compression the fiber/resin mixture may not deform uniformly as intended [13]. Due to the entanglement of fibers, fibers are likely to stay in place during compression while only resin flows resulting in non-uniform distribution of fibers. Achieving uniform distribution of fiber volume fractions over the entire area of the composite part is thus crucial to ensure overall structural stability.

In this study, the effect of the fiber entanglement was investigated for different fiber lengths: 6.25, 12.5, 25, 50, and 100 mm. Preliminary entanglement analysis was performed by spraying chopped glass fibers with an emulsion binder via a down-sized lab-scale experimental apparatus. An emulsion binder is generally used for manufacturing chopped glass fiber mats, as a matrix. Specimens of chopped glass fiber were solidified using an emulsion binder and soaked in warm water (35 °C) prior to the experiment in order to remove any unwanted interfacial strength between the fiber and the binder [14].

The viscoelastic nature of the uncured composite part comprises two dominant forces upon compression molding: friction force (fiber entanglement) and viscous force (matrix). In order to analyze and model the fiber separation of the uncured composite mixture upon compression molding for various fiber lengths and matrix viscosities, the friction coefficient between the two glass fiber strands was obtained.

The effect of the matrix viscosities on the fiber entanglement upon compression molding was examined by using a newly built experimental apparatus. Moreover, visualization of the fiber volume distribution before and after compression molding was shown in MATLAB. It clearly has shown that the MATLAB code with the data acquired by experiments could be proposed as a modeling tool to predict the uniformity of fiber volume at the final stage of LFSM.

2. Methodology

2.1. Materials and experimental apparatus

Acrylic water-soluble emulsion binder (binder to water ratio, 10:90) was supplied by Sunwoo Chem. Co. Ltd, South Korea. A glass fiber roving with a filament diameter of 13 μm and linear mass density of 2400 g/m was purchased from Jushi Group Co. Ltd, South Korea.

The lab-scale LFSM experimental apparatus used in this study was designed and experimented with in our previous work. The

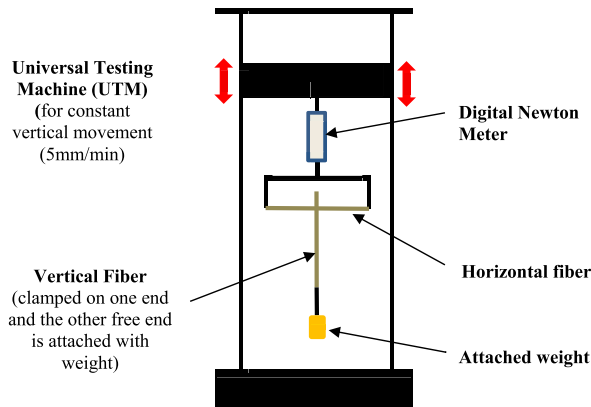


Fig. 2. Fiber-on-Fiber friction measurement set-up.

experimental apparatus consists of a fiber chopper gun mounted at an angle to spray chopped glass fibers into a resin stream driven by a piston in a cylindrical tank, as illustrated in Fig. 1. The piston driving the resin flow and the fiber chopper gun are operated independently using air pressure to precisely meet the fiber volume fractions of the composite part. The fiber chopper gun consists of two rollers rotating toward each other. While one roller rotates freely, the other is controlled using air pressure. The length of the chopped fiber is determined by the number of blades inserted. For instance, using one blade results in a chopped fiber length equivalent to a 100 mm circumference, while two blades yield a 50 mm length, and so on. It's worth noting that the margin of error for length accuracy is minimal, staying within 2 %, which ensures a high level of precision. The apparatus was accurately designed such that the speed of the system in horizontal coordinates would be controlled to match the speed of the resin flow. Furthermore, the apparatus consists of electromagnets in order to sustain the mechanism onto the steel plate upon compression molding [7].

Instead of dispensing a low viscosity resin such as epoxy or polyurethane from the apparatus, an emulsion binder with a binder to water ratio of 10:90 was filled in the chamber. Once the mixture of fiber and binder with weight ratio of 50:50 was sprayed onto the mold (300 × 300 × 4 mm³), it was placed in an oven at 70 °C for approximately 3–4 h in order to evaporate the water content present in the part. The role of the binder was to emulate the effect of the resin and to keep the fibers in place to evaluate the degree of entanglement.

2.2. Tensile test

The degree of entanglement was assessed by measuring the tensile behavior using the universal testing machine (LLOYD Instrument, LR50K, 1 kN load cell, Bognor Regis, UK) at a test speed of 3 mm/min. To avoid limiting any potential entanglement effect from longer fibers, samples of 120 (length) × 40 (width) × 4 (thickness) mm³ were cut from each specimen. In order to avoid any potential interfacial strength between the binder and the fiber, samples were soaked in warm water (35 °C) for 24 h prior to the experiment. In this manner, most of the emulsion binder could be removed while maintaining the structural geometry of the sample intact. Upon completion of the tensile test, the rate of the deformation was analyzed using the exponential decay function as shown in Eq. (1) [15].

$$F(x) = a + be^{-kx} \tag{1}$$

where k is the exponential decay rate of b . Because a , b , and k are instantaneous rates, the units are equal: time^{-1} [15]. By performing the tensile test, fiber elongation from the peak load to zero was recorded in order to observe the effect of fiber entanglement.

2.3. Fiber-on-fiber friction measurement

In the early stage of the experiment, the degree of fiber entanglement was considered to be increasing as the fiber length was increased. It was clear that the presence of the friction force between the entangled structure of fibers was resisting the separation upon compression molding. In order to undertake modeling of the viscoelastic property of the uncured long fiber composite part for future research, the friction force between the two in-contact glass fiber strands was measured via UTM as shown in Fig. 2.

Visualized in Fig. 2, the vertical fiber was hung with a defined weight at its free end. While the vertical fiber was stationary, the horizontal fiber moved up and down while the two were in contact.

The frictional force between two in-contact fibers was obtained using the power law of friction as shown in Eq. (2) [16].

$$F = aP^n \tag{2}$$

where F denotes the frictional force, P is the normal load, and a and n are frictional constants. The force equilibrium of the two in-contact fibers is depicted in Fig. 3.

The relation between the work of friction and the friction force due to vertical displacement was evaluated. Following equations

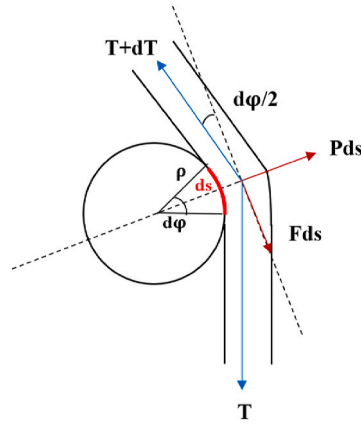


Fig. 3. Force equilibrium of the two in-contact fibers.



Fig. 4. (a) Original microscopy image, (b) grey-scaled image obtained from MATLAB, (c) result of Canny's Edge detection method, images showing the counting of the number of (d) nodes and (e) fibers.

(Eq. (3 – 5)) were used to determine the coefficient of friction [16].

$$Fds = (T + dT)\cos\left(\frac{d\varphi}{2}\right) - T\cos\left(\frac{d\varphi}{2}\right) \cong dT \tag{3}$$

where T and $T + DT$ are the tensile forces acting at the ends of element ds .

$$Pds = (T + dT)\sin\left(\frac{d\varphi}{2}\right) - T\sin\left(\frac{d\varphi}{2}\right) \cong T d\varphi \tag{4}$$

where P is the reaction per unit length of the fiber.

$$F = a\left(\frac{mg}{\rho}\right)^n \tag{5}$$

Where, this equation states that for given values of a and n , friction forces of different fibers are equal if the ratio of attached weight to the fiber radius is constant.

2.4. Image processing

In order to quantitatively analyze the effect of fiber entanglement in relation to fiber length, image processing was employed. The aim of the image processing was to determine the number of fiber intersections (nodes) per individual fiber. The effect of entanglement arises from a crossover between fibers creating friction force between the fibers [7]. For image processing, samples of different fiber lengths were first scanned through confocal microscopy (Lext OLS4100 Olympus). The size of the scanned samples was set to $150 \times 150 \text{ mm}^2$ for all fiber lengths in order to obtain a full image of the longest sample (100 mm in length).

Image processing was performed using MATLAB. In order to qualitatively obtain the edges of individual fibers, the ‘‘Canny Edge Detection’’ method was implemented [17]. Images from the microscope were first converted to greyscale images (from 0 to 255), as shown in Fig. 4(a and b). The images were converted because the use of RGB input data is not eligible for any calculation. The noise present in the grey-scaled image was then reduced and smoothed using a 5×5 Gaussian filter (the first step of the ‘‘Canny Edge Detection’’ method) [17]. This noise-filtering method was applied using the following Eq. (6) [18].

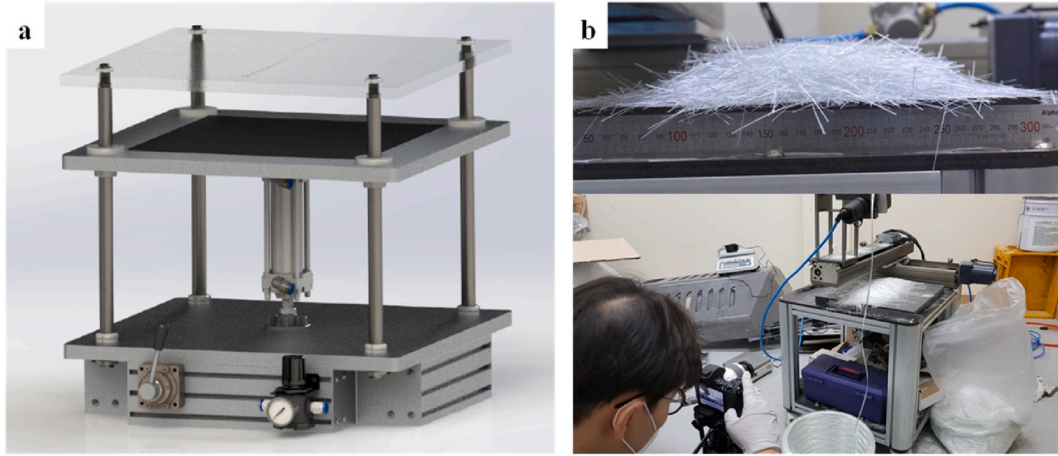


Fig. 5. (a) Design and the built experimental apparatus for observing the effect of fiber entanglement upon compression and (b) cross-section of the photographed uncured mixture.

$$G(x, y) = \frac{1}{2\pi\sigma^2} \exp\left[-\frac{x^2 + y^2}{2\sigma^2}\right] \quad (6)$$

The standard deviation for controlling the smoothening degree is σ . After removing the noise from the image, the edge strength was determined by taking a gradient of the image using the Sobel operator, which measures the 2-D spatial gradient [19]. This allows the magnitude of the absolute gradient at each point to be determined. The edge gradient was estimated using Eq. (7).

$$\text{Edge Gradient, } G = \sqrt{G_x + G_y} \quad (7)$$

where G_x and G_y are the gradients in the x and y planes, respectively. From the values of gradients found in the x and y planes, individual edge directions (angles, θ) can be estimated with Eq. (8) [19],

$$\tan \theta = \frac{G_y}{G_x} \quad (8)$$

After determining the edge direction, it was then altered such that it can be traced in an image. This was processed by simplifying edge angles (direction) to four distinct angle segments: 0° , 45° , 90° and 135° . Upon simplification, edges were traced along their directions and any edge with a non-maximum value was suppressed and set with a pixel value equal to zero [19]. By undertaking hysteresis thresholding for the very last stage of the process, any non-edge pixel was removed and finally, the real edges were distinctively marked.

Through these processes, clearer and more distinct fiber edge profiles were obtained, as shown in Fig. 4(c). The image was then used to count the number of intersections (nodes) and the number of fibers for all samples with different fiber lengths. The process was applied using the concepts of 2D convolution and matrix filters [20]. Examples of node and fiber counting are provided in Fig. 4(d and e).

In order to verify the results from actual images obtained through confocal microscopy, virtual fiber mats with well-dispersed and randomly oriented fibers of different lengths were generated by the computer. From the virtual mats thus generated, the number of nodes per fiber for all different fiber lengths was evaluated and compared with the results from the actual images.

2.5. Fiber flow distance measurement upon compression molding

During the preliminary stage of the entanglement observation, the effect of the resin viscosity was neglected. As the experiment proceeded, it was found that using a low viscous resin can cause uneven distribution of fibers due to the resin readily flowing through the fibers upon compression molding. Increasing the viscosity to the point where the viscous force is predominant over the adhesion force between the fibers will result in evenly distributed fibers across the composite part. Nevertheless, increasing the viscosity can never be good since insufficient fiber impregnation will likely occur.

Observation of the fiber entanglement during the compression molding was undertaken using the experimental apparatus as shown in Fig. 5(a). It is comprised of two horizontal plates; the top plate is transparent acrylic with scales fixed in position and the bottom plate moves vertically in which the speed and the pressure are controlled via air.

The fiber content was fixed at 30 wt% for fiber lengths of 12.5, 25, 50, and 100 mm. For each fiber length, the experiment was undertaken for viscosities of 10, 30, 100, 350, and 1000 cps. Silicon oil was used as a matrix since numerous repetitions were required. The mixture of the chopped glass fiber and the silicon oil was performed using the LFSM apparatus. The air pressure and the closing speed of the plate were set as 10 bar and 12 mm/s, respectively.

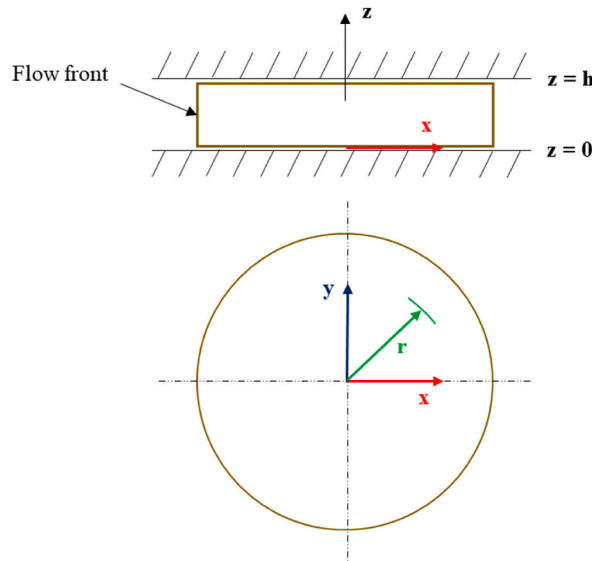


Fig. 6. Coordinates of circular-shaped part upon compression molding.

During the compression. Videos were taken perpendicular to the plate and the relative distance of the fiber was measured by using the scales marked on the plate.

The experimental fiber flow distance was compared to the calculated theoretical fiber flow distance. The theoretical values were calculated as follows,

The equation of motion for a single fiber can be written as Eq. (9) [21],

$$\frac{w_f}{g} \frac{dv_f}{dt} = C_D \frac{\gamma_m}{2g} (v_m - v_f)^2 a_f + w_f \frac{\gamma_f - \gamma_m}{\gamma_m} \cos \theta - f_f \tag{9}$$

where f_f is the mutual restraint force due to frictional and inter-wound forces of fibers (shape of fiber, fiber content, molding process variables), θ is the angle between gravity and the direction of flow, γ_f and γ_m are the specific weight of fiber and matrix respectively, C_D is the drag coefficient, v_f and v_m are the velocity of fiber and matrix respectively, w_f is the weight of fiber, and a_f is the cross-sectional area of fiber.

In the case of a Newtonian fluid, the drag coefficient can be approximated as [22],

$$C_D = \alpha \bullet Re_f^{-\beta} \tag{10}$$

And the Reynolds number,

$$Re_f = \frac{(v_m - v_f) d_f \rho_m}{\mu_m} \tag{11}$$

where d_f is the diameter of fiber, ρ_m and μ_m are the density and viscosity of matrix, respectively.

To simplify the geometry of the fiber for modeling, it was considered a sphere. From Eqs. 9–11, the following Eq. (12) for the fiber velocity is obtained [22].

$$v_f = v_m - k_{sp} \frac{\gamma_f d_{fs}^2}{\mu_m} \tag{12}$$

where k_{sp} is the coefficient of separation and is defined as Eq. (13) [22],

$$k_{sp} = \frac{f_f}{18 j_{sp} w_f} \tag{13}$$

where j_{sp} is the correction factor for the drag.

During the experiment, a small batch of resin and fiber mixture was sprayed onto a steel plate before it was visually observed upon compression force. The geometry of a small batch is very similar to a circular slab shape as shown in Fig. 6.

The average matrix velocity v_m and the viscosity of matrix μ_m can be obtained using the momentum, continuity, and rheological equations, Eq. 14–16 [22].

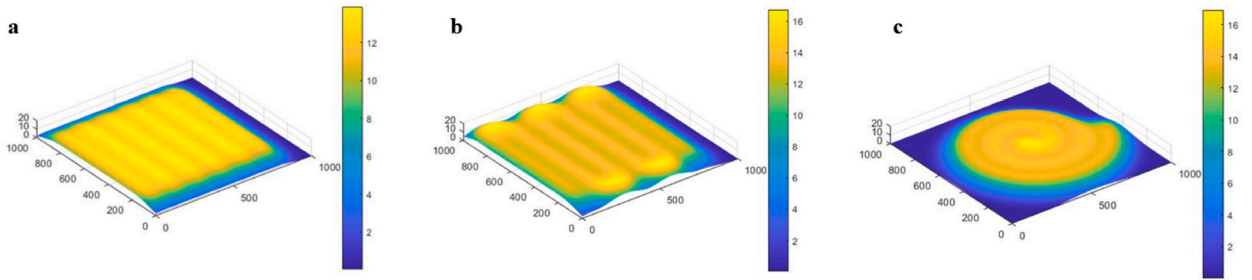


Fig. 7. Spray patterns for, a) line b) zig-zag c) Spiral.

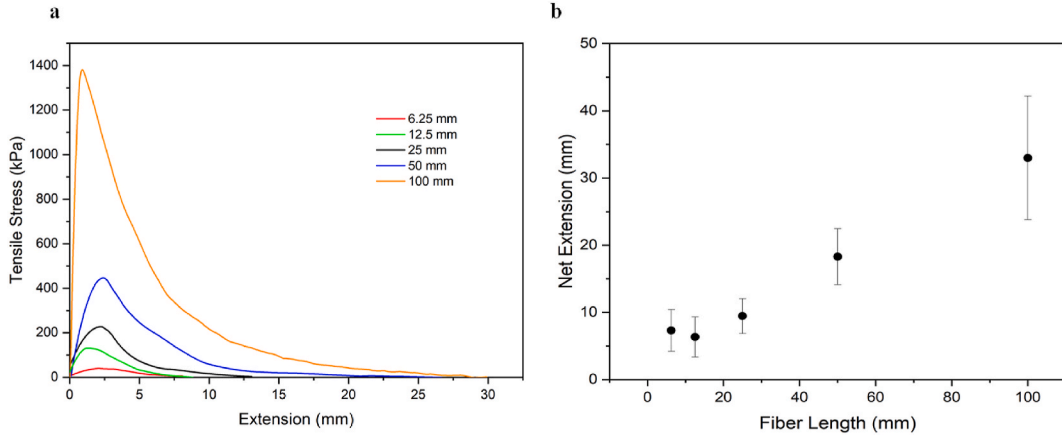


Fig. 8. (a) Tensile load versus elongation for different fiber lengths and (b) net extension of fibers from the peak load.

$$\bar{v}_m = \frac{\dot{h}r}{2h} \tag{14}$$

$$\mu_m = K_m \left(C \frac{\dot{h}}{h^2} r \right) \tag{15}$$

The flow distance of fiber considered as a sphere during molding can be written as,

$$S_f = r_0 \left(\sqrt{\frac{h_0}{h}} - 1 \right) - K \frac{\gamma_f d_{fs}^2}{\mu_m} \left(\frac{h - h_0}{h} \right) \tag{16}$$

The equivalent diameter of the sphere, d_{fs} was determined by relating the volume of fiber equal to sphere.

2.6. Computational modeling of LFSM

It was easily noticeable that the cross-section of the sprayed mixture of fiber and the resin was similar to a parabola with the highest fiber volume fraction at the center of the spray. In order to computationally model the sprayed uncured mixture, the cross-sectional view of the part was photographed and analyzed as shown in Fig. 5(b). A ruler was placed beside the sprayed part in order to obtain the shape by converting it from pixels to mm. The irregularity of the constructed profile was standardized by using the Gaussian function as shown in Eq. (17) [23].

$$f(x, y) = A \exp - \left(\frac{(x - x_0)^2}{2\sigma_x^2} + \frac{(y - y_0)^2}{2\sigma_y^2} \right) \tag{17}$$

where A is the amplitude, x_0 and y_0 are the center, σ_x and σ_y are the x, y spreads of the distribution.

Through standardization to a normal distribution function, a simplified shape of the sprayed mixture was achieved. Stacking of the 2D Gaussian function into a 3D plot was made and the overlap between each sprayed line was added together as it would be the same case in the actual experiment. The distance between the centers of the spray was set initially as 200 mm and it was possible to manipulate depending on the processing conditions.

Table 1
 Constants for the exponential decay rate function for all fiber lengths under tensile loading.

Exponential Decay, $F(x) = a + b e^{-kx}$				
Fiber Length (mm)	a	b	K (rate)	R-square
6.25	-1.76	134	-0.376	0.99
12.5	-32.3	306	-0.3	0.99
25	-9.21	405	-0.28	0.98
50	0.592	871	-0.25	0.99
100	18.6	1751	-0.21	0.99

Fig. 7 displays three distinct spray patterns. These patterns were developed to evaluate their potential impact on fiber volume distribution for potential future uses. In Fig. 7, patterns a, b, and c correspond to line, zig-zag, and spiral sprays, respectively. From the previous experiment and by using the theoretical values of fiber flow distances, visual observations of the fiber volume from compression molding were possible which will be discussed in the later section.

3. Results and discussion

3.1. Tensile test

Degrees of fiber entanglement in the fiber mats were assessed by the tensile test using a universal testing machine. Unlike the failure of composite structures, in which a sudden fracture causes a dramatic decrease in the tensile strength, the tensile strength of fiber mat with emulsion binder as the matrix was expected to decrease asymptotically with the tensile strain. This is because the interfacial strength of the fiber and the binder was minimized by soaking in warm water (35 °C) for 24 h prior to the experiment.

As shown from the trend of the loading curve for all fiber lengths in Fig. 8(a), tensile load asymptotically decreased, after an increase to a peak value at the start of the experiment. Unlike fiber breakage in other composite materials, fibers in the mat disentangled over time. The rate of disentanglement depends on the fiber length because the entanglement of longer fibers is significantly larger than that of short fibers.

The interface between the fibers and the binder may exhibit a small interfacial strength when the tensile load is first applied and when it approaches the peak load. Therefore, the effect of the entanglement was evaluated by the net extension of the fiber from the peak load to zero, as shown in Fig. 8(b). Assuming that the effect of the interfacial strength is negligible, the net extension increased non-linearly with increasing fiber length. The net extension of the shortest fiber (6.25 mm) and the longest fiber (100 mm) was 7.3 mm and 33 mm, respectively. For 100 mm fiber, the net extension was almost 4.5 times the shortest fiber experimented with in this study. This particular investigation can be thought of analogously to a situation when undertaking compression molding of resin-impregnated chopped glass fibers. As the length of the glass fiber increases, it becomes difficult to break the adhesion forces from the fiber bundle due to the entanglement as shown in the test. Since fiber disentanglement is critical to achieving even fiber volume distribution throughout the composite part, the viscosity of the resin for LFSM must carefully be selected. Disentanglement of the fiber bundle can only be achieved if the viscous force from the resin is predominant over the entanglement force [7].

The maximum tensile loading increases with the fiber length. However, the entanglement phenomenon can be viewed in terms of the tensile load reduction rate over longitudinal elongation. From Fig. 8(a), the reduction rate from the peak load to zero for all fiber lengths was examined and evaluated as in Table 1. The rate of the tensile load reduction was analyzed by using the exponential decay function.

Due to the increase in fiber entanglement with increasing fiber length, the rate at which the fiber bundle separates clearly decreases with increasing fiber length. It was found that the rate at which the fiber bundle separated decreased by 44 % going from the shortest to the longest fiber. In addition, the exponential decay function fitted very well with the actual data, showing R-square values of 0.99 for all fiber lengths. To use long fiber spray-up molding as a composite fabrication method, an in-depth understanding of the existence of fiber entanglement forces is required. Hence, the matrix properties must carefully be selected such that uniformity of fiber volume distribution throughout the composite part can be achieved.

3.2. Fiber-on-fiber friction measurement

In the conducted experiment, the objective was to precisely characterize the frictional behavior between individual fibers. To achieve this, a controlled setup was employed where two fiber strands were brought into contact. The vertical displacement of the fiber-to-fiber contact point was set at 150 mm, with a corresponding horizontal displacement of 61 mm relative to the initial hanging position. The angle between the fibers measured 22.1° with an additional weight of 23 g attached. Moreover, it was determined that the average frictional force between the fibers was quantified at 0.015 N hence the calculated friction coefficient was, 0.16.

The significance of this coefficient lies in its direct applicability to the ongoing research. Specifically, it serves as a key parameter in predicting the flow behavior of fiber bundles during the compression molding.

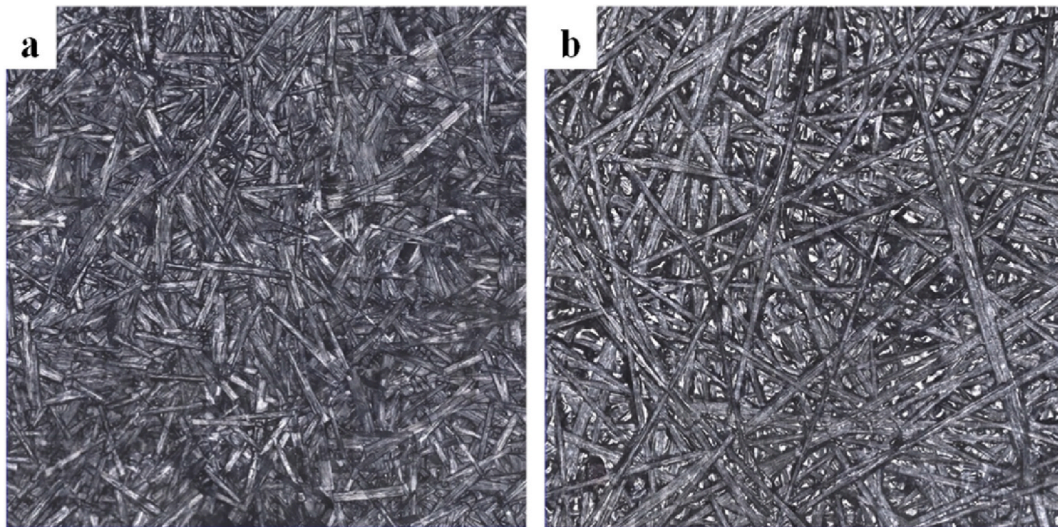


Fig. 9. Microscopic images of fiber mats with fiber lengths of a) 6.25 mm b) 100 mm.

Table 2

Number of nodes from the actual and virtual samples obtained using the microscopic image processing.

Fiber Length (mm)	Actual No. of nodes/fiber	Virtual No. of nodes/fiber
6.25	0.877	0.756
12.5	2.15	2.42
25	8.81	7.84
50	16.94	16.6
100	23.5	20.3

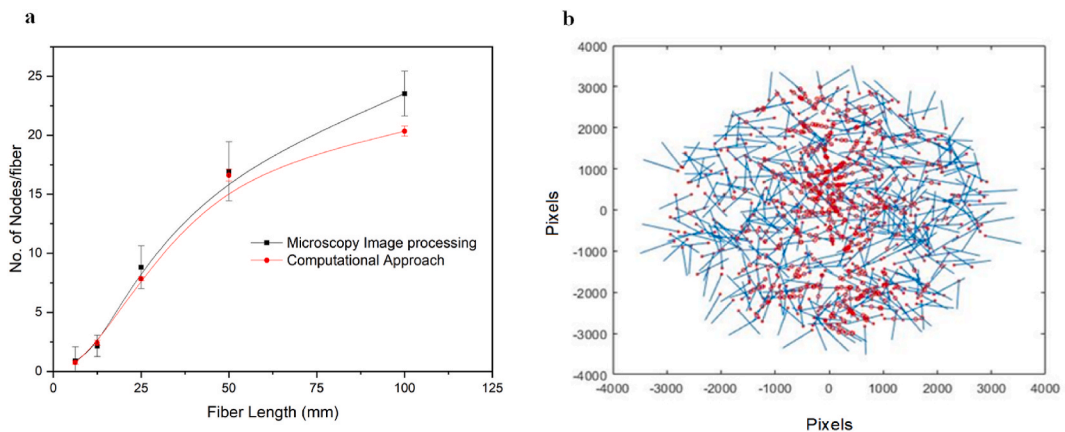


Fig. 10. (a) Numbers of nodes per fiber for different fiber lengths and (b) number of nodes counted for the virtual mat generated by computer.

3.3. Image processing

The main scope of the image processing was to determine the number of fiber intersections (nodes) per fiber to model the effect of fiber entanglement in future studies. The first step of the process was to analyze the samples of the chopped glass fiber with an emulsion binder as the matrix for various fiber lengths. The images were taken using confocal microscopy and then examined using the Canny edge detection method. Considering the limitations of using only six different fiber lengths for the experiment, a MATLAB code was generated such that it can distribute any specified number of fibers and lengths in a random orientation to a specified area. Furthermore, the number of nodes per fiber was evaluated for both methods.

Examples of the microscopic images obtained are shown in Fig. 9(a and b). Even without any analysis, the amount of intersection

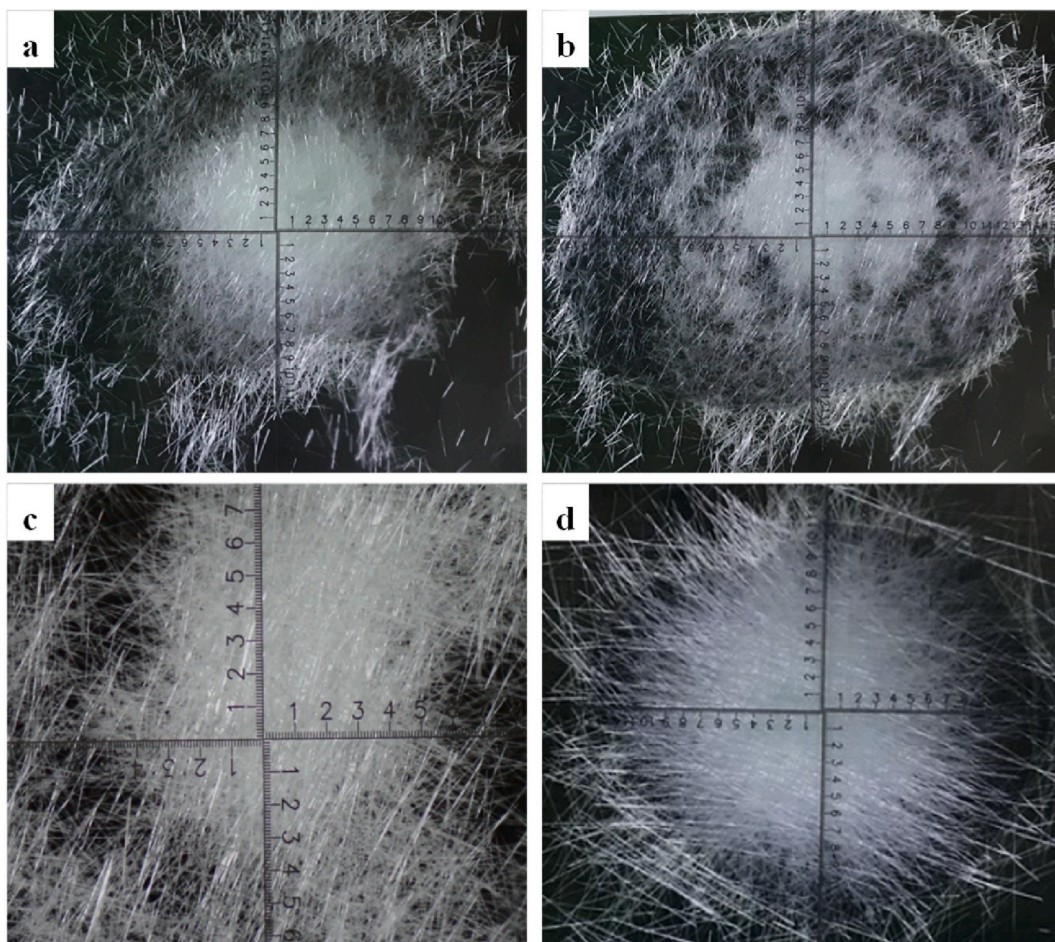


Fig. 11. (a) Before compression for 12.5 mm fiber and after compression for (b) 12.5 mm, (c) 25 mm, (d) 100 mm fibers.

per fiber can be observed to be significantly larger for samples of 100 mm fiber length than that for 6.25 mm. The number of nodes per fiber strand determined from the microscopic analysis is shown in Table 2. The average number of nodes per fiber for 6.25 mm and 100 mm was 0.877 and 23.5, respectively. Fiber length of 100 mm had almost 27 times more cross-section points between fibers in comparison to 6.25 mm fiber.

The results show that the number of nodes per fiber increases as the fiber length increases. This explains that the reason for the fiber entanglement phenomenon is fiber ensnaring. Similar results were obtained for the virtual fiber mat as shown in Table 2. In the virtual mat, 500 fiber strands were randomly distributed over a radius of 3000 pixels and the number of nodes was counted within a given area of 6000×6000 pixels.

As shown in Fig. 10(a), results from the actual samples and the virtual mats match closely. However, the results of the actual sample provided a slightly larger number of nodes per fiber. This may be due to two reasons. Firstly, the confocal microscope takes 2D images of the samples, which means that some parts of intersections would not be actual overlaps (fibers on the top and bottom). In the computer-generated virtual mat, however, the number of nodes per fiber is accurately determined for all fiber lengths, as shown in Fig. 10(b). This probability increases as the fiber length increases. Second and finally, since the images are processed through various filters, a few parts of the images are read as intersections even though they are not actual overlaps. Despite the difference between the two methodologies, they provided similar results in that the number of nodes per fiber saturates as the fiber lengths are increased. This is because the effect of the entanglement for long and discontinuous fibers of lengths above 100 mm becomes very close to that of continuous fibers. As previously mentioned, as the length of the chopped strands of glass fiber becomes extremely long, almost 90 % of the strength of continuous fiber can be attained regardless of the type of matrix [8].

3.4. Fiber flow distance upon compression molding

It was clear from the experiment that the shortest fiber of 12.5 mm had the lowest dependence on viscosity of the matrix. As shown in Fig. 11(a and b), fiber entanglement breakage easily occurs despite a low viscous matrix. Moreover, the fiber spreading was significantly enhanced when the viscosity was further increased. The effect of fiber entanglement was clearly shown when the fiber

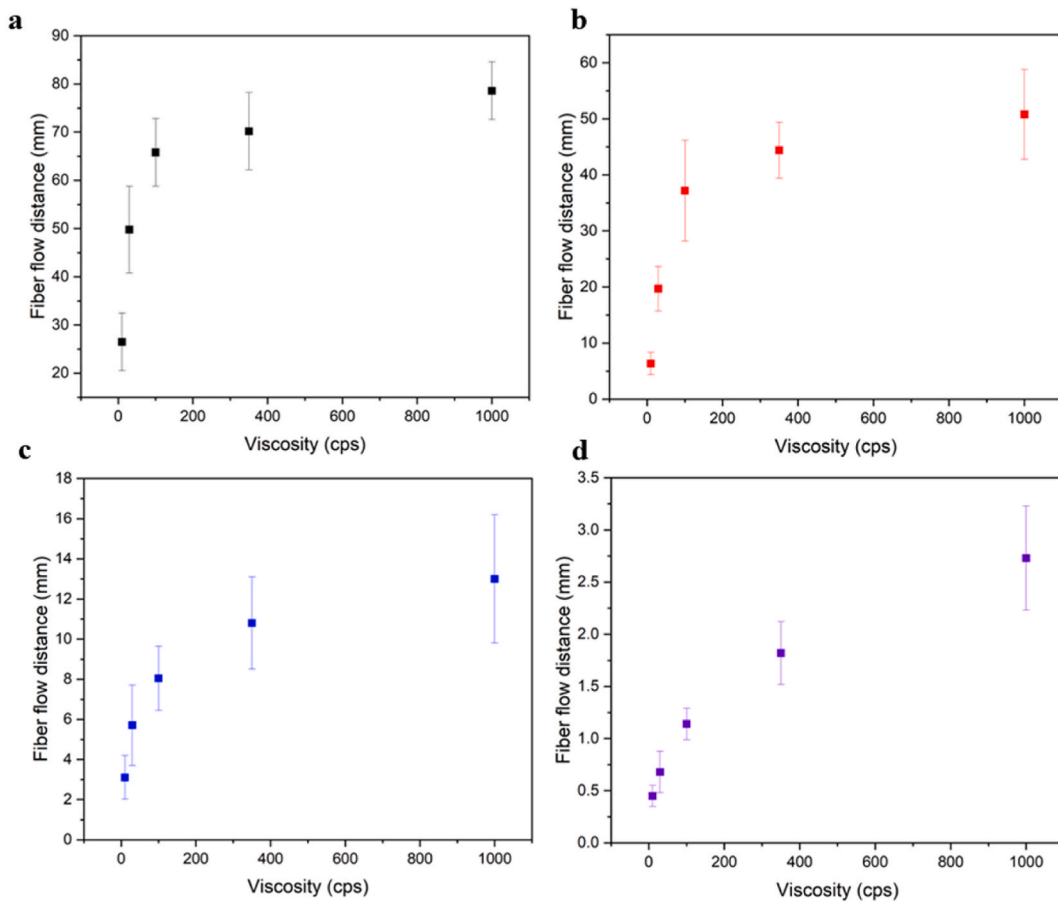


Fig. 12. Fiber flow distance with different matrix viscosities for (a) 12.5 mm, (b) 25 mm, (c) 50 mm, (d) 100 mm fibers.

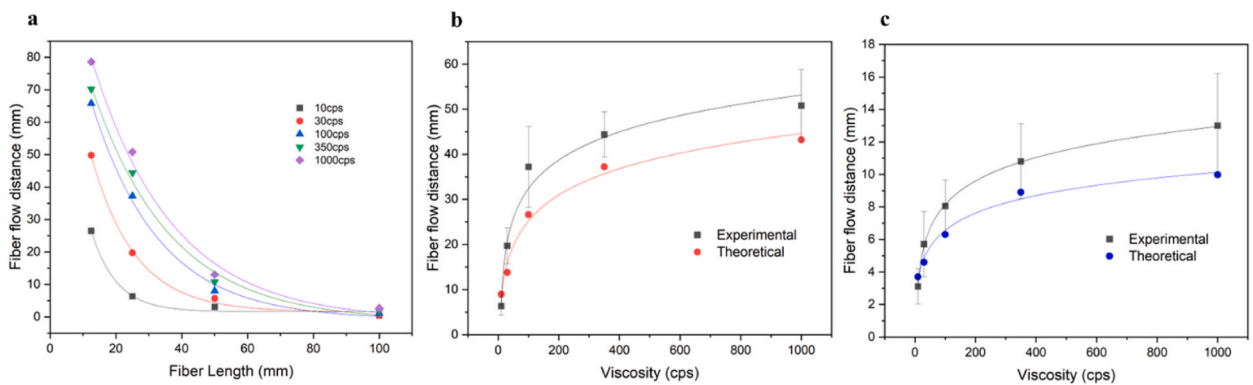


Fig. 13. (a) Fiber flow distance depending on matrix viscosity for increasing fiber length and comparison between experimental and theoretical fiber flow distances for (b) 25 mm fiber and (c) 50 mm fiber.

length was increased. A larger degree of viscosity had to be increased for breakage of fiber agglomeration as the fiber length increased as shown in Fig. 11(c and d). For the same viscosity of 350 cps, the break-up of the fiber bundle happens for 25 mm but not for 100 mm fiber.

Since the experiment was undertaken for a small batch of a mixture, the spreading of the fibers towards the outer edges was greater over the center part. In the actual experiment however, the outer edges will overlap with thus if a separation of entanglement occurs, fibers from individual outer edges of each spray line will gather to match closely to the fiber volume at the center line of the spray.

Fiber flow distances for different viscosities of the matrix of 12.5, 25, 50, and 100 mm are shown in Fig. 12(a-d). The increase of

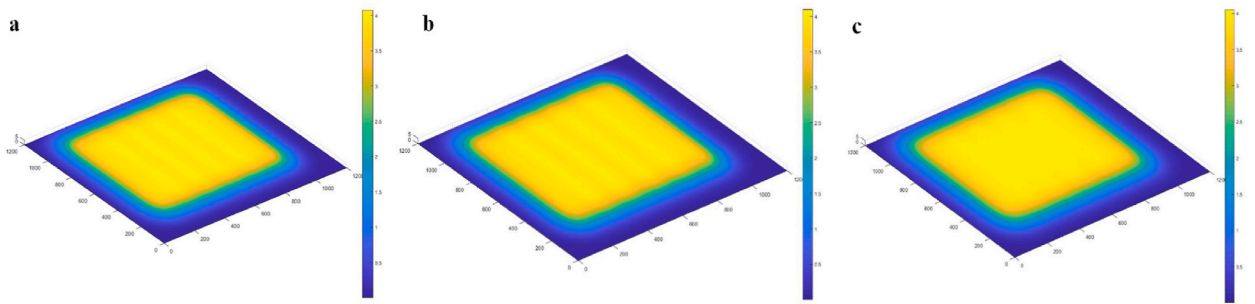


Fig. 14. 25 mm fiber straight line spray pattern for, a) 30 cps, b) 100 cps, c) 350 cps.

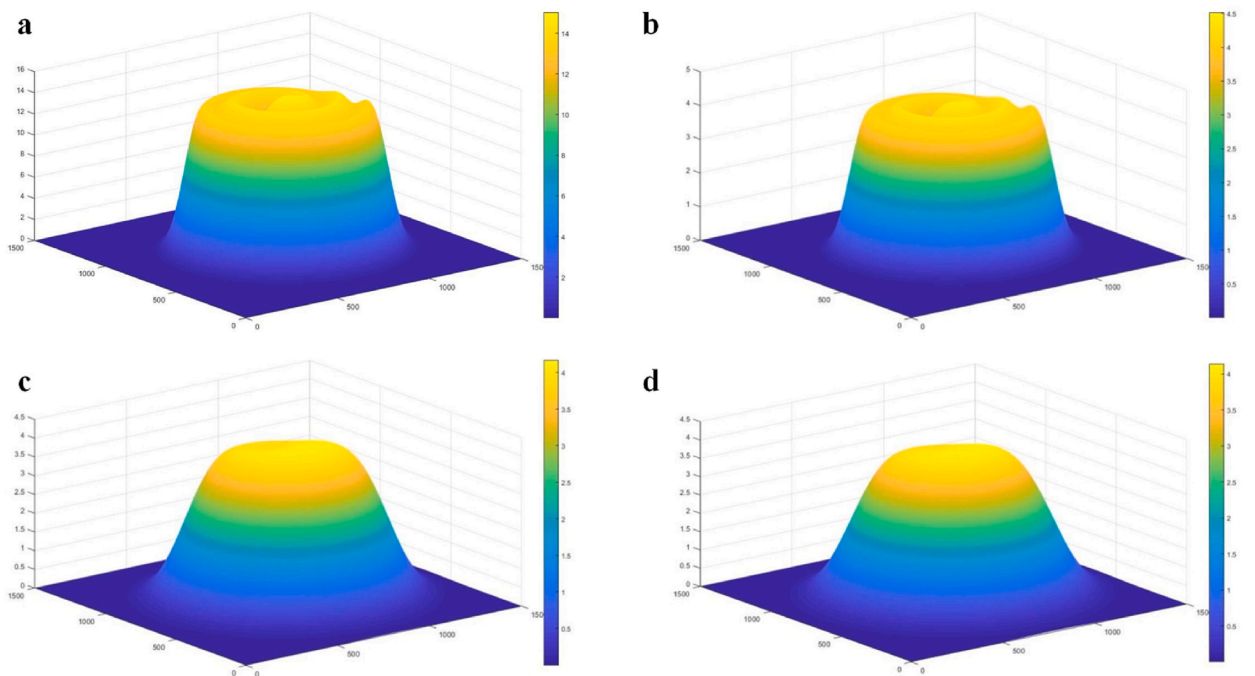


Fig. 15. 50 mm fiber spiral spray pattern (a) before compression and after compression for (b) 100 cps, (c) 350 cps, (d) 1000 cps.

fiber flow distance over increasing viscosity asymptotically saturates. This was mainly because the viscous force of the matrix became predominant over the entanglement force ultimately. Hence for each fiber length, it was possible to determine the optimum viscosity which could result in uniform fiber volume distribution while achieving sufficient impregnation.

Fig. 13(a), shows that the fiber flow distance depends on matrix viscosity with increasing fiber length. As the fiber length increases, the flow distance asymptotically decreases despite an increase in the matrix's viscosity. Such phenomena are due to the fact that the effect of the entanglement becomes similar to that of a continuous fiber for a length above 70 mm. Accordingly, it would be very difficult to manufacture composites with such extreme length as problems with non-uniform fiber volume distribution and insufficient impregnation may occur.

The fiber flow distance from the experimental and theoretical values was compared for 25 and 50 mm fibers as shown in Fig. 13(b and c), respectively. The values have shown that they have similar trends over an increasing viscosity. However, it can be clearly seen that the difference between the two results increases as the resin viscosity is increased. This is due to the fact that since the experimental apparatus can have initial acceleration of the plates during closing (speed controlled via air) and the acceleration term is neglected during the theoretical calculation. This factor has seen to contribute to a greater degree as the fiber length was increased and it can be seen that at 1000 cps, theoretical and experimental values for 25 and 50 mm differ by 18 and 30 %, respectively.

3.5. Computational modeling of LFSM

In the preliminary stage of LFSM modeling, it was assumed that the shape of the sprayed mixture (fiber and resin) was normally

distributed along its center line. With the obtained spread radius upon compression, it was possible to visualize the outcomes after when it was compression molded.

In Fig. 14, a straight-line spray pattern for 25 mm fibers is presented, with viscosities of 30, 100, and 350 cps represented as a, b, and c respectively, after the part underwent compression molding. It can be clearly seen that using the resin viscosity of 350 cps had the most uniformly distributed fiber through the thickness. Fig. 15 showcases different views of a 50 mm fiber. Fig. 15(a) represents the fiber before compression molding, while b, c, and d correspond to after compression molding with viscosities of 100, 350, and 1000 cps, respectively. In the case of the fiber length of 50 mm, the viscosity had to be at least above 350 cps for uniform distribution. Moreover, increasing the viscosity to 1000 cps did marginally increase the uniformity but chances of insufficient impregnation were very high.

4. Conclusion

Overall, the effect of the fiber entanglement was analyzed for fiber lengths ranging between 6.25 and 100 mm. Tensile testing results revealed that it took greater force and time to disentangle fibers with increasing fiber length. Additionally, the microscopic images of the samples and MATLAB analysis showed that the number of nodes (intersections) per fiber increased with increasing fiber length. The result of the increased number of intersections leads to greater friction between fibers; hence a greater entanglement effect was observed for longer fibers. Similar results were obtained with the computational approach using virtual and randomly drawn fibers in MATLAB. Finally, through the viscoelastic analysis upon compression molding, reliable data were obtained to predict and visualize the outcomes for the final composite part. The methods and data revealed in this study offers new insight into the effect of fiber entanglement and provides simulations of the outcomes on the quality of the composite part for reducing the number of unnecessary experiments.

Data availability statement

Data will be made available on request.

CRediT authorship contribution statement

Ji Ho Jeon: Conceptualization, Formal analysis, Writing – original draft. **Chang Ki Yoon:** Data curation, Software, Visualization. **Ying-Jun Quan:** Investigation. **Jun Young Choi:** Validation, Writing – review & editing. **Sungjin Hong:** Investigation. **Woo Il Lee:** Project administration, Supervision. **Kui-Kam Kwon:** Investigation. **Sung-Hoon Ahn:** Funding acquisition, Resources, Supervision.

Declaration of competing interest

The authors declare that they have no known competing financial interests or personal relationships that could have appeared to influence the work reported in this paper.

Acknowledgment

This work was supported by the National Research Foundation of Korea (NRF) grant funded by Korea government (MSIT) [NRF-2021R1A4A2001824, NRF-2021R1A2B5B03087094]

Appendix A. Supplementary data

Supplementary data to this article can be found online at <https://doi.org/10.1016/j.heliyon.2023.e22170>.

References

- [1] D. Abraham, S. Matthews, R. McIlhagger, A comparison of physical properties of glass fibre epoxy composites produced by wet lay-up with autoclave consolidation and resin transfer moulding, *Compos. Appl. Sci. Manuf.* 29 (7) (1998) 795–801.
- [2] J.Y. Choi, et al., Current Applications and Development of Composite Manufacturing Processes for Future Mobility, *International Journal of Precision Engineering and Manufacturing-Green Technology*, 2022.
- [3] C. Garschke, et al., Out-of-autoclave cure cycle study of a resin film infusion process using in situ process monitoring, *Compos. Appl. Sci. Manuf.* 43 (6) (2012) 935–944.
- [4] H.M. Yoo, et al., Influence of non-reactive epoxy binder on the permeability and friction coefficient of twill-woven carbon fabric in the liquid composite molding process, *Appl. Sci.* 10 (20) (2020) 7039.
- [5] F. Wittemann, et al., Injection molding simulation of short fiber reinforced thermosets with anisotropic and non-Newtonian flow behavior, *Compos. Appl. Sci. Manuf.* 124 (2019), 105476.
- [6] D.S. Kim, C.W. Macosko, Reaction injection molding process of glass fiber reinforced polyurethane composites, *Polym. Eng. Sci.* 40 (10) (2000) 2205–2216.
- [7] J.H. Jeon, et al., Assessment of long fiber spray-up molding of chopped glass fiber reinforced polydicyclopentadiene composites, *Fibers Polym.* 21 (5) (2020) 1134–1141.
- [8] L. Harper, et al., Fiber alignment in directed carbon fiber preforms—a feasibility study, *J. Compos. Mater.* 43 (1) (2009) 57–74.

- [9] Z. Hesabi, B. Majidi, J. Aghazadeh, Effects of Stacking Sequence on Fracture Mechanisms in Quasi-Isotropic Carbon/epoxy Laminates under Tensile Loading, 2005.
- [10] Y. Wan, J. Takahashi, Tensile and compressive properties of chopped carbon fiber tapes reinforced thermoplastics with different fiber lengths and molding pressures, *Compos. Appl. Sci. Manuf.* 87 (2016) 271–281.
- [11] C. Jiang, et al., Experimental study on the mechanical properties and microstructure of chopped basalt fibre reinforced concrete, *Mater. Des.* 58 (2014) 187–193.
- [12] D.G. Seong, et al., Influence of fiber length and its distribution in three phase poly(propylene) composites, *Compos. B Eng.* 168 (2019) 218–225.
- [13] A.G. Adeniyi, et al., A review of coir fiber reinforced polymer composites, *Compos. B Eng.* 176 (2019), 107305.
- [14] E. Gellert, D. Turley, Seawater immersion ageing of glass-fibre reinforced polymer laminates for marine applications, *Compos. Appl. Sci. Manuf.* 30 (11) (1999) 1259–1265.
- [15] P. Rovira, R. Rovira, Fitting litter decomposition datasets to mathematical curves: towards a generalised exponential approach, *Geoderma* 155 (3–4) (2010) 329–343.
- [16] A. Alirezazadeh, et al., Fiber-on-fiber friction measurement using hanging fiber method, *J. Text. Inst.* 109 (5) (2018) 636–646.
- [17] J. Canny, A computational approach to edge detection, *IEEE Trans. Pattern Anal. Mach. Intell.* (6) (1986) 679–698.
- [18] C.-X. Deng, G.-B. Wang, X.-R. Yang, Image edge detection algorithm based on improved canny operator, in: 2013 International Conference on Wavelet Analysis and Pattern Recognition, IEEE, 2013.
- [19] B. Green, Canny Edge Detection Tutorial, vol. 6, Retrieved, 2005. March, 2002.
- [20] S. Kim, R. Casper, Applications of Convolution in Image Processing with MATLAB, University of Washington, 2013, pp. 1–20.
- [21] H. Hojo, et al., Separation of matrix and fibers during molding of long fiber-reinforced thermoplastics, *Composites'86: Recent Advances in Japan and the United States* (1986) 605–612.
- [22] H. Hojo, E. Kim, K. Tamakawa, The fibre content distribution of compression molded long fibre-reinforced thermoplastic products, *Int. Polym. Process.* 1 (2) (1987) 60–65.
- [23] N. Hagen, E.L. Dereniak, Gaussian profile estimation in two dimensions, *Applied optics* 47 (36) (2008) 6842–6851.